Article ID: 1000-7032(2023)12-2085-13

Inkjet Printing Quantum Dot Films: Solvent Selection Strategies for Jetting Inks

OU Jiaqi, PENG Zengyi, WANG Junjie,
LI Danyang, SONG Jianing, PENG Junbiao*

(*State Key Laboratory of Luminescent Materials and Devices, South China University of Technology, Guangzhou* 510641, *China*)

* *Corresponding Author, E-mail: psjbpeng@scut. edu. cn*

Abstract: The morphology of quantum dots (QDs) films fabricated by inkjet printing makes a marked impact on the performance of multi-layer photoelectronic devices, such as quantum dot light emitting diodes, where coffee-ring and bulge phenomena behave as the typical poor morphology types. Realizing high-quality QDs films through droplet modulation is key to the development of QDs electroluminescent displays. Ink engineering has been proven effective in adjusting the film morphology. However, a well-tailored ink with precise rheological properties to eliminate coffee ring or bulge requires multiple time-consuming experimental attempts, resulting in lower working efficiency. In this work, we sought to directly bridge the gap between the rheological properties of solvents and the profiles of inkjet-printed QDs films with post-mortem film analysis and machine learning methods adopted for mutual proof. With red QDs as the solutes, and alkanes or chain esters as solvents, work on unitary-solvent and binary-solvent ink systems was investigated to find out that generally, the boiling point of the used solvent displayed significant importance higher than that of surface tension or viscosity in both unitary and binary systems. Specifically, the film profile was closely related to the solvent with a higher boiling point in binary systems and uniform films were revealed. A boiling point range of 250−265 ℃ for the solvent in the unitary-solvent ink system or for the higher-boiling-point solvent in the binary-solvent ink systems can promisingly result in uniform films after drying.

Key words: quantum dot ink; inkjet printing; solvent; machine learning

CLC number: O482. 31 **Document code**: A **DOI**: 10. 37188/CJL. 20230228

喷墨打印量子点薄膜:墨水溶剂的选择策略

欧家琦, 彭曾一, 王俊杰, 李丹阳, 宋家宁, 彭俊彪*

(华南理工大学 发光材料与器件国家重点实验室, 广东 广州 510641)

摘要: 喷墨打印制备的量子点(Quantum dots, QDs)薄膜形貌对多层发光器件的性能影响显著(如量子点发光二极管),其中咖啡环与拱状形貌是典型的薄膜均匀性问题,通过液滴调控实现高质量QDs薄膜是发展量子点电致发光显示的关键。研究工作表明,通过溶剂实施的墨水调控被证明是改变沉积薄膜形貌的有效手段。然而,优化出可消除咖啡环或拱状形貌的墨水流变参数往往需要大量耗时的实验,墨水配制筛选效率低。本研究基于薄膜形貌分析结合机器学习方法,试图将溶剂流变参数与喷墨打印QDs薄膜形貌直接联系起来,并以红光QDs为溶质,以烷烃或直链酯类为溶剂,研究发现通常使用的一元溶剂和二元溶剂体系中,所使用溶剂的沸点比表面张力或粘度参数对薄膜沉积形貌的影响更加显著,在二元溶剂中薄膜形貌与沸点较高的溶剂组分

收稿日期: 2023-10-07; **修订日期**: 2023-10-17
基金项目: 广东省重点研发计划(2022B0303010001); 国家重点研发计划(2022YFB3603103); 国家自然科学基金(62074059)
Supported by Key R&D Plan of Guangdong Province(2022B0303010001); National key Research and Development Program of China(2022YFB3603103); National Natural Science Foundation of China(62074059)

密切相关。为得到厚度均匀的平整薄膜,建议一元溶剂墨水体系的溶剂或二元溶剂墨水体系中较高沸点的溶剂的沸点范围为 250~265 ℃。

关 键 词:量子点墨水;喷墨打印;溶剂;机器学习

1 Introduction

Inkjet printing (IJP) of quantum dots (QDs) droplets is gaining popularity due to its promising potential in displays[1]. QDs have emerged as an alternative to the traditional non-emissive color filters in LCDs or the self-emissive functional layers in OLEDs due to their striking properties including narrow-spectrum luminescence, high quantum yield and solution processability[2-7]. Inorganic colloidal QDs are the most commonly used type of QDs in inkjet printing QLEDs, including CdSe, InP, and CdTe[8-9]. Polymer-based QDs and small-molecule-based QDs are also frequently used in this field, known for their high stability and high efficiency, respectively[10-11]. Poly(9,9-dioctylfluorene-co-bis-N,N-(4-butylphenyl)-bis-N,N-phenyl-1,4-phenylenediamine)(PFB) is a typical example of the former, while 4,4′-bis(N-carbazolyl)-1,1′-biphenyl (CBP) is a typical example of the latter. IJP boasts several operational advantages over spin-coating and vacuum-evaporation, such as precise patterning, large-area film producibility and low material wastage[3,12-14]. To ensure uniform light emission as well as efficient carrier transportation in high-quality optoelectronic devices, uniform thickness and smooth surface are required for each functional layer, rather than the typical unideal coffee-ring or bulge morphology[15]. The solvent evaporation and solute deposition of sessile QDs droplets on substrates determine the film profile[16-18] . There are a plethora of factors that can influence the dynamics of droplet drying[19]. Specifically, we are interested in how the solvent rheological properties can alter the deposited film profile and eager to find out the more efficient means to tailor it, which is the motivation for this research.

Micro-droplet drying is a very complex process, and its simplification is therefore crucial for efficiency optimization. It can be summarized that vapor, liquid and solid phases may influence the final film morphology of a picoliter QDs droplet by changing the interfacial mass transfer fluxes and contact line motions[20], which in turn affects the internal flow pattern of the droplet, as presented in Fig. S1. Specifically, solvent engineering has been applied in a wide range of material systems as it can significantly adjust evaporation kinetics[16-18,20-22]. Essentially, it takes advantage of the differences in rheological properties of solution between different regions within a droplet to control the internal flow behavior during drying, thus altering the solute distribution to form the desired films[20,23]. The widespread use of solvent modulation is based on its operational ease and remarkable impacts, as a small amount of another solvent could cause dramatic effects[24-26]. However, the droplet drying process is extremely complex due to a variety of physical mechanisms and a number of factors involved, making solvent modulation simple to carry out but difficult for precise regulation. In most cases, boiling point (T_{bp}), surface tension (γ) and viscosity (η) are the three key rheological parameters that have the most significant influence on the droplet drying process[18], and clarifying the specific roles and contribution weights of the three parameters to film formation is of vital importance for the efficient formulation of QDs inks, the preparation of thin films with uniform thickness and flat surface, and the processing of high-performance quantum dot light-emitting diodes(QLEDs)[27]. However, the direct connections between film quality and these parameters still need to be studied.

Besides the fruitful studies on unitary-solvent inks, several pairs of binary solvents were reported to produce uniform films for QLEDs in recent years, hugely boosting the eternal quantum efficiency[28-33]. They discovered that preventing interlayer erosion[30-31,33], balancing capillary outward flow and Marangoni flow[28,32,34] and controlling the three-phase

line motions[29] are the keys to affect the film morphology and thus the efficiency of the device. However, ink engineering, the crucial process to realize the large-area and low-cost fabrication of cutting-edge devices, still largely depended on recipes developed by manual trial and error based on semi-empirical theories in most of the previous research. Specifically, multiple effecting factors and corresponding film-forming mechanisms were studied and presented from a qualitative point of view, which brought confusion and difficulties to efficient ink tailoring. Therefore, clarifying the functions of each solvent component and the order of priority of diverse factors makes sense and matters a lot.

In this work, we tried to bridge the gap between the rheological properties of solvents and the film profiles of inkjet-printed colloidal QDs droplets using post-mortem film analysis, *in-situ* observation of the drying process and machine learning. Temporal observations of the drying process and theoretical calculations were main analyzing tools, while machine learning models based on data simulation were involved to help support conclusions to reduce labor and time costs. By integrating experiments and modeling for cross-check and mutual proof, we correlated the rheological properties of solvents and final film profiles of inkjet-printed QDs drops, expecting to offer a more efficient insight into the selection of the solvent components to mitigate coffee rings or bulges.

2　Experiment

2.1　Materials

The red QDs were purchased from Shenzhen Planck Innovation Technology Co., Ltd., China. n-Octane and n-Hexadecane with purity better than 99% were purchased from Sigma-Aldrich Inc., Germany. n-Nonane, n-Decane, n-Undecane, n-Dodecane, n-Tridecane, n-Tetradecane, n-Pentadecane, bicyclohexane, methyl dodecanoate, methyl tridecanoate, amyl hexanoate, butyl hexanoate, methyl decanoate, chlorobenzene and decalin were purchased from Aladdin Ltd., China. Heptylcyclohexane, nonylcyclohexane and hexyl hexanoate were purchased from Macklin Inc., China. Octylcyclohexane was purchased from Tokyo Chemical Industry Co., Ltd., Japan. All the solvents were filtered through a 45-μm polyethersulfone syringe filter for organic solution samples before used.

2.2　QDs Ink Preparation

QDs powder was dissolved with an appropriate amount of the modulated solvent to make a concentration of 30 mg/mL. The fresh QDs ink was shaken evenly for uniform dispersion and filtered through a 0.45-μm polytetrafluoroethylene filter to remove impurities. The QDs ink was then loaded into a cartridge for printing. Therefore, the QDs ink consists of a volatile liquid or a mixture of two volatile liquid and QDs with an average size of (9.377 ± 1.544) nm(Fig. S2).

2.3　QDs Film Preparation

The QDs ink droplets with various formulations were inkjet-printed at ambient temperature by a piezoelectric printer(JetLab II) with a 20-μm nozzle from MicroFab Technologies, Inc., USA. The voltage waveform and negative pressure of the printer were adjusted to generate a string of vertical drops. The printer parameters and calibrate position were set to fix the printing patterns on the perfluoropolyethers(PFPE) substrate with surface energy of 45–50 mN/m. After printing, the samples were dried out at room temperature and were taken off from the platform for further characterization.

2.4　Characterizations

The shape and size distribution of QDs were determined from a transmission electron microscopy (TEM, JEM-1400 Plus) from JEOL Ltd., Japan. The luminescence spectrum was recorded by a spectroscopy(QE Pro) from Biaoqi Electronics Technology Co., Ltd., China. The viscosity of the QDs inks or pure solvents was obtained by a rotational viscometer(LVDV-I+) from Brookfield AMETEK Inc., USA, while the surface tension was measured by an optical tensiometer (Theta Lite Model TL 100) with its corresponding software OneAttension from Biolin Scientific, Sweden. The post-mortem film profiles of QDs films were observed by a 3D laser confocal scanning microscope(LEXT OLS5000) from Olympus Optical

Co. Ltd., Japan. The normal and fluorescent images of the QDs films were captured by a polarized light microscope (Axiolab 5 with Axiocam 105 Color Microscope Camera) from Carl Zeiss Microscopy GmbH, Germany in normal mode and fluorescent light mode respectively. All the measurements were carried out at temperature about 25 ℃ and humidity about 55%.

2.5 Profile Datasets

Fig. 1 shows the quantitative parameters measured from a film profile captured by a 3D laser confocal scanning microscope. In Fig.1 (a), central height (H) refers to the average height of the area with a length equal to 10% of diameter(D) in the middle of the film. As mentioned above, the typical unideal film morphology may be coffee rings or bulges. The coffee ring effect describes an unideal profile of the film where most of the solutes migrate to the rim and accumulate there, resulting in a typical concave volcano-like profile[21, 35]. On the contrary, bulges result from the accumulation of QDs in the middle, which causes a convex mountain-like profile[16,35]. Therefore, surface curvature A shown in Fig. 1(b), which was obtained from a quadratic function $f(x) = Ax^2 + Bx + C$, was defined to characterize the convexity of the film surface in this work. Four sample groups of film surface data, which implied concave(b1), flat-ununiform(b2), flat-uniform(b3) and convex(b4) film respectively, were fitted into the function for suitability check, whose results are presented in Tab. S1. The b2, b3 and b4 groups displayed perfect fitting with the coefficient of determination R^2= 1.000 while the b1 group performed slightly badly with R^2 = 0.498, which might be attributed to a mismatch between the smooth fitted curve and the original steep inner side of the ring structure. However, these results proved sufficient feasibility for quadratic function in surface profile characterization, where A>4E-6 indicates concave while A<−4E-6 indicates convex and the range 4E-6≥A≥−4E-6 indicates flat surface with a spin-coated film as the standard one (Fig. S3).

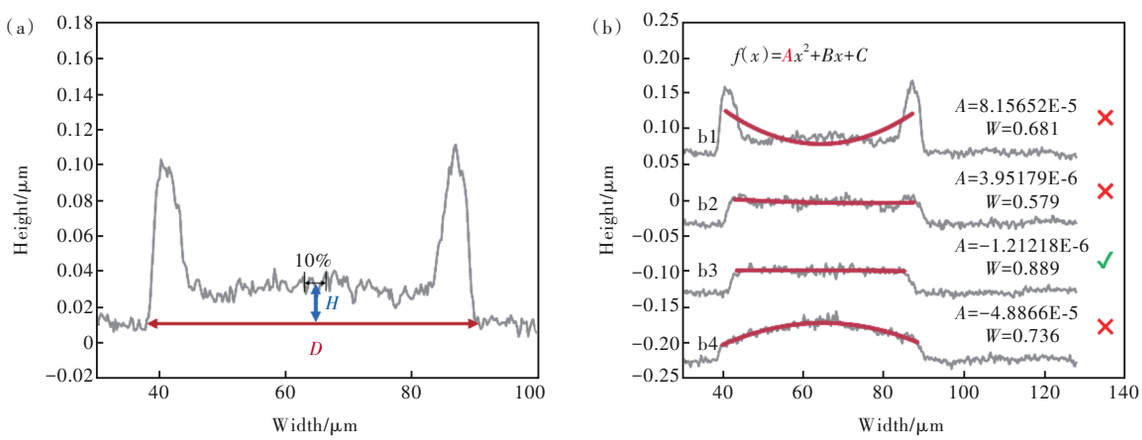

Fig.1 Quantitative parameters of a deposited film morphology. (a)Central height H, diameter D. (b)Surface curvature A.

For the unitary-solvent ink system, boiling point, surface tension and viscosity of pure solvent were used as input variables to build a Random Forest Model for predicting the surface curvature of the film profile. For a binary-solvent ink system, the difference between boiling points (ΔT_{bp}), surface tension ($\Delta\gamma$) and viscosity ($\Delta\eta$) of the minor solvent (30% vol) and the major solvent (70% vol) were used as input variables defined as equation (1), (2) and (3) respectively:

$$\Delta T_{bp} = T_{bp\text{-}minor} - T_{bp\text{-}major}, \quad (1)$$

$$\Delta\gamma = \gamma_{minor} - \gamma_{major}, \quad (2)$$

$$\Delta\eta = \eta_{minor} - \eta_{major}. \quad (3)$$

2.6 Model Construction

Furthermore, four datasets consisting respectively of 120 pairs for unitary-solvent system (Tab. S2), 56 pairs for binary-solvent system using decalin as the major solvent (Tab. S3), 120 pairs for binary-solvent system using bicyclohexane as the major solvent (Tab. S4) and 64 pairs for binary-solvent system using octylcyclohexane as the major solvent

(Tab. S5) were constructed.

Firstly, we constructed Random Forest Models to calculate feature importance[36-37]. The pseudocode for this process is presented below:

(1) Initialize an empty dictionary to store feature importance scores.

(2) For each tree in the forest:

a. Traverse the tree and calculate the total decrease in node impurity (weighted by the probability of reaching that node) for each feature.

b. Add the feature importance scores to the dictionary.

(3) Normalize the feature importance scores by dividing them by the sum of all feature importance scores.

(4) Return the normalized feature importance scores.

Secondly, we used the Random Forest Models to make predictions. The pseudocode for this process is presented below[38]:

(1) For each tree in the forest:

a. Traverse the tree and predict the outcome for the test data.

b. Store the predicted outcome.

(2) Calculate the mode of the predicted outcomes across all trees.

(3) Return the mode as the final prediction.

In our work, all the datasets were then independently divided into training and test sets at a ratio of 8-2 and used for the construction and evaluation of the prediction model.

3　Results and Discussion

The rheological properties of the prepared solvents were divided into four groups, as shown in Tab. S6, S7, S8 and S9, corresponding respectively to a unitary-solvent system and three binary-solvent systems with decalin (DCL), bicyclohexane (BCH) and octylcyclohexane (OCH) as the major solvent respectively. No nozzle clogging was observed during all the printing processes, which indicated that the boiling points of the chosen solvents were high enough to ensure a stable droplet formation over a long time period. Fig. S4, S5, S6 and S7 show the corresponding deposited film profiles from which all the data were measured according to the measurements depicted in Fig. 1. Information about diameter D, and central height H could be found in Fig. S8 and S9 for unitary-solvent ink system and binary-solvent ink systems respectively.

All the unitary solvents were divided into four group based on their chemical structure, corresponding to cyclohexane-X (sample #1-sample #3), cyclohexane-alkane (sample #4-sample #6), alkane (sample #7-sample #10) and ester (sample #11-sample #15), according to the tags noted in Tab. S6. Since solvents of the same group have similar structures and properties, one solvent was chosen from each group: bicyclohexane, n-octyl cyclohexane, n-hexadecane, and methyl dodecanoate. The morphology and particle size distribution of the nanoparticles were measured by TEM. As shown in Fig. S10(a), S10(b), S10(c), S10(d), after being dissolved in the above four solvents, the size of the quantum dots did not change significantly compared to that in n-octane (D_a = (9.377 ± 1.544) nm). It should be noted that after being dissolved in methyl dodecanoate, the particle size distribution range of the quantum dots was slightly wider (Fig. S10(e)), which is because quantum dots tend to aggregate slightly in ester solvents with weak polarity (Tab. S6), but still within a good range of solubility. These histograms proof good interaction between quantum dots and the solvents. Fig.2(a)-(c) show the relationship of surface curvature A with T_{bp}, γ, and η of pure solvent in the unitary-solvent system respectively. It was found that A decreased as T_{bp}, γ, and η increased in every single group. However, despite different chemical structures, A decreased as the T_{bp} increased as a whole, while A did not exhibit such obvious correlations with γ or η (Fig. 2(b) and (c)). Therefore, T_{bp} was deluded to be the key parameter deciding A of the deposited film profile.

Generally, T_{bp} of solvent controls the evaporation rate, while γ decides wetting and η determines the internal friction of solvent[21]. The evaporation rate relates closely to the speed of capillary compensation flow inside the droplet[20]. The faster the

evaporation, the faster the liquid flows[16]. Besides, wetting affects liquid flow with adhesive force between droplet and substrate[39]. The lower the adhesive force, the faster the liquid flows. Moreover, internal friction suppresses flowing[40]. The lower the friction, the faster the liquid flows. Therefore, lower $T_{bp,}$ higher γ and lower η can promote flowing. Fig. S11 shows the temporal evolution for ink droplets with unitary solvents of (a) bicyclohexane(sample # 2), (b) n-tetradecane (sample #8) and (c) octylcyclohexane(sample #5) respectively taken by an optical microscope. Two changing processes of three-phase contact line, sticking and sliding, were depicted in Fig. S11, whose durations were then denoted correspondingly as t_{stick} and t_{slide} presented in Fig. 2(d). Previous work has reported that the descending of droplet surface during the initial period of drying is attributed to a large amount of solvent dismissing into the air[20, 41-43]. Therefore, with the corresponding T_{bp} of the three solvents increasing, the t_{stick} lengthened. Interestingly, the second stage was different from what had been observed before[18], the droplet neither dried out with a pinned rim nor slid on the substrate. Instead, the rims of the three droplets all slid right on the deposited QDs film and the droplet ultimately dried out in the middle of the film. This scenario may be attributed to the relatively low surface energy of PFPE substrate(45-50 mN/m), which enabled easier depinning for the rim. Several rules for substrate selection were listed before[12,28,32], including solvent orthogonality and good wettability emphasized the most, based on which an ultra-thin PFPE was chosen as the interfacial layer between the transporting layer and the QDs emitting layer. Firstly, PFPE lacks solubility in organic solvents, preventing interfacial erosion between different functional layers. Secondly, despite low surface energy compared to the usual transporting layer, PFPE can provide sufficient wettability for the solvents selected in this work because a substrate can be fully wetted once the surface tension of the liquid is lower than that of the substrate[23,44-45]. Besides, this smaller gap between the two surface tensions enables weaker pinning of the three-phase contact line, thus accelerating in the depinning process. Herein, with γ and η rising in turn, their influence on the flow ability of liquid canceled out, resulting in a similar t_{slide} for different solvents. Specifically, Fig. 2(d) shows that the t_{stick} is longer than the $t_{side.}$ During the t_{stick}, the dissipative force of the solvent molecule into the ambient air is quite violent and drags the solvent to the rim, thus hugely affecting the locations of solutes at the beginning. However, in the bulk liquid phase, viscosity has a small impact because the droplet is

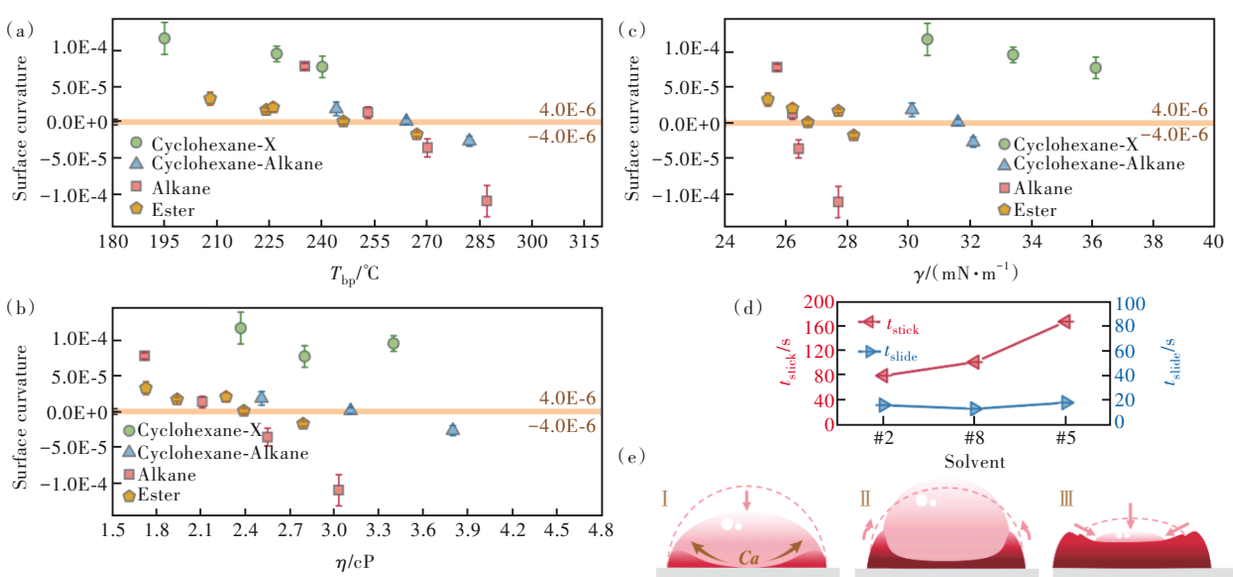

Fig.2 Experimental data and a drying diagram of unitary-solvent system. Relationships between A and T_{bp}(a), γ(b), and η(c) of pure solvent. (d)Sticking time t_{stick} and sliding time t_{slide} of the three ink droplets during drying. (e)Schematic diagram of the three stages of drying a QDs ink droplet. *Ca* refers to capillary flow inside the droplet.

not flowing at this moment. Additionally, due to the violent evaporation at the rim, the solvent displays weaker wetting on the substrate. As time passes, this force gradually reduces, but the amount of solvent in the droplet is far less than at the beginning, which is unable to move the solutes despite constriction to the middle of the film during t_{side}.

Herein, three stages of evaporation of an ink droplet on a PFPE substrate were depicted in Fig. 2(e). In stage Ⅰ, the rim of the droplet pins, and the height of the liquid surface drops because of the capillary compensation flow towards to rims inside the droplet during evaporation. This stage, who lasts for a longer time, is mainly controlled by the boiling point and also affected by the surface tension. The lower the T_{bp}, the higher the evaporation rate, and further the shorter the t_{stick}; with the same T_{bp}, the lower the γ, the smaller the contact angle, and further the shorter the t_{stick}. In stage Ⅱ, the droplet overcomes pinning. At this point, the droplet has to overcome the obstruction on the rim, *i. e.*, the real-time deposited QDs. Therefore, a solvent with lower viscosity with stronger flow ability is easier to break free from pinning. In stage Ⅲ, the three-phase contact line of the droplet slides on the deposited QDs film until the droplet dries out. To maintain the spherical shape, the rim of the ink droplet slides inward driven by surface tension[18], whereas viscosity controls the ability of a liquid to flow[28,46]. Herein, this stage is controlled by surface tension and viscosity, the higher the γ or the lower the η, the shorter the t_{slide}. Considering the longer t_{stick} compared to t_{slide}, T_{bp} was considered the most important parameter to determine the ultimate deposited profile of QDs film in the unitary-solvent system, followed by γ and η in sequence. Additionally, within all the inks prepared, QDs ink with octylcyclohexane (T_{bp} = 259 ℃, γ = 31.6 mN/m, η = 3.11 cP) as the unitary solvent could be used to print flat film.

Fig. 3 shows the relationships of A with ΔT_{bp}, $\Delta\gamma$, and $\Delta\eta$ of pure solvents, respectively, in binary-solvent systems. Generally, A decreased as the ΔT_{bp}, *i. e.*, the T_{bp}^{*}, increased (Fig.3(a)). For DCL-based group, concave film appeared mostly when $\Delta T_{bp} \leqslant$ 44.10 ℃ while convex film appeared when $\Delta T_{bp} \geqslant$ 58.00 ℃ without a flat film achieved. For BCH-based group, concave film appeared when $\Delta T_{bp} \leqslant$ 15.00 ℃ while convex film appeared when $\Delta T_{bp} \geqslant$ 29.30 ℃, and a flat film was achieved when ΔT_{bp} = 20.00 ℃. For OCH-based group, flat films were formed when ΔT_{bp} = −20.00 ℃ or ΔT_{bp} = −5.00 ℃, and convex film appeared mostly when $\Delta T_{bp} \geqslant$ 5.50 ℃ without a concave film recorded. On the contrary, A did not exhibit obvious correlations with $\Delta\gamma$ or $\Delta\eta$ (Fig. 3(c) and (d)). Boltzmann sigmoidal fitting was further adopted to evaluate the correlations of A with

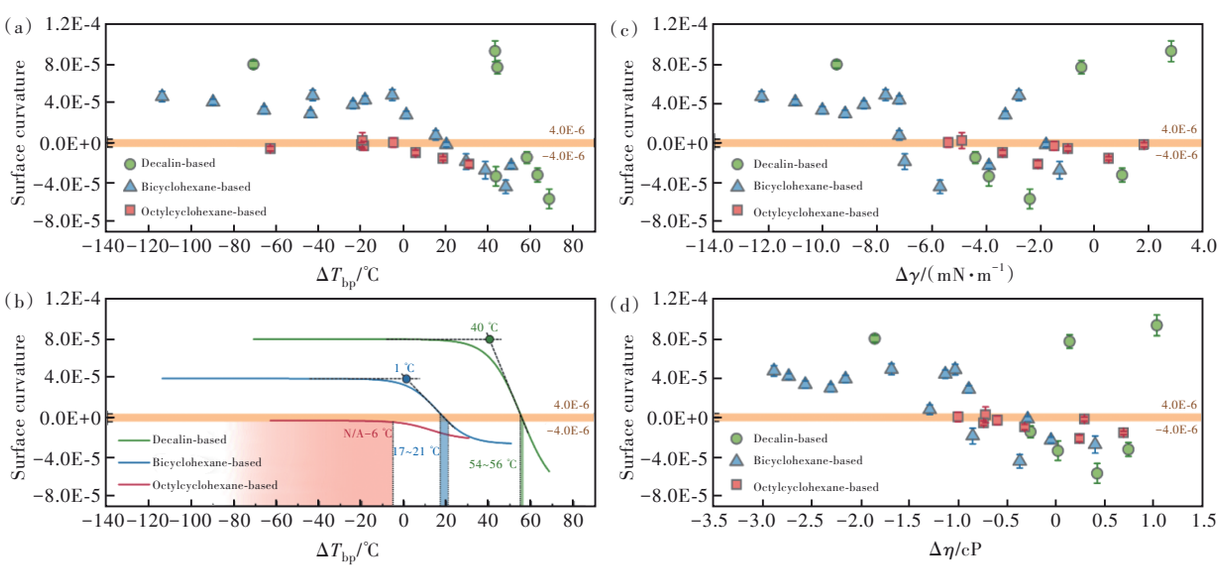

Fig.3　Experimental data and fitting functions of binary-solvent systems. Relationships between A and ΔT_{bp}(a), $\Delta\gamma$(c), and $\Delta\eta$(d) of binary solvents. (b)Fitting Boltzmann sigmoidal functions to A-ΔT_{bp} datasets.

ΔT_{bp}, $\Delta\gamma$, and $\Delta\eta$ respectively, whose results are presented in Tab. S10. A strong correlation of A with ΔT_{bp} can be found in each group, although the respective Chi-Sqr value varied as the result of different major solvents used. In comparison, the correlation of A with $\Delta\eta$ was weak, because only the BCH-based A-$\Delta\eta$ dataset can be fitted into convergence with a less desirable Chi-Sqr value. Furthermore, the correlation of A with $\Delta\gamma$ was considered to be the weakest, given none of the A-$\Delta\gamma$ datasets could be fitted into convergence. Fig. 3(b) presents the A-ΔT_{bp} Boltzmann sigmoidal fitting lines. On the DCL-based line and BCH-based line, an inflection ΔT_{bp} of 40 ℃ and 1 ℃ existed, respectively, indicating that the film profile started to change from a deep concave towards flat and further convex. However, there was no such an inflection point on OCH-based line because none of binary solvent in this group resulted in concave film in experiments. Preliminarily, it could be deducted from the fitting line three corresponding ideal ΔT_{bp} ranges (Tab. 1), which were 54–56 ℃ for the DCL-based group, 17–21 ℃ for the BCH-based group, and N/A ~6 ℃ for the OCH-based group. Combined with the corresponding T_{bp}, the ideal T_{bp}^* ranges were 250–252 ℃, 256–260 ℃ and <253 ℃. Noticeably, a major solvent with a higher T_{bp} can tolerate a broader range of boiling point differences for good film formation.

It is therefore concluded that the main parameter determining A is the boiling point T_{bp}^* of the minor solvent and its ideal range is between 250–260 ℃. Combing with the results of the unitary-solvent system, it was found that it is the higher-boiling-point solvent in binary-solvent systems determines the ultimate deposited film morphology, because a unitary solvent with a T_{bp} of around 260 ℃ can also result in flat film. However, it is preferred that T_{bp}^* be higher than that of the major solvent to accelerate the whole drying rate because the small amount. It can stay until the last stage of evaporation despite of smaller amount and thus function to smoothen the ultimate film profile. Furthermore, a low-boiling-point major solvent with good solubility is preferred because it can shorten the overall evaporation duration. With T_{bp} is less than 260 ℃, flat films are more likely to be realized when the range of T_{bp}^* is between 250–260 ℃.

Tab. 1 Properties of three kinds of major solvent and the respective ideal range of boiling point of the minor solvent according to Boltzmann fitting results

Major solvent	T_{bp}/℃	γ/(mN·m^{-1})	η/cP	Inflection ΔT_{bp}/℃	Ideal ΔT_{bp} range/℃	Ideal T_{bp}^* range/℃
DCL	196.0	30.6	2.4	40	54 ~ 56	250 ~ 252
BCH	239.0	33.4	3.4	1	17 ~ 21	256 ~ 260
OCH	259.0	31.6	3.1	N/A	N/A ~ 6	< 253

Random forest(RF), a machine learning prediction model, incorporates the importance of input variables for prediction[36]. It yields quantified information about the features and their contribution to the prediction *via* multiple tree models as shown in Fig. S12. Therefore, RF models were utilized to perform importance analysis and prediction on film profile, *i.e.* A value, in this work. In addition, R^2 and root mean square error(RMSE) were used as evaluation metrics for the model performance.

Fig. 4 shows the results of the feature importance analysis in each system, where the inserts represent the performance in predicting A. The inserted line plots show that the training and test sets had similar trends. For the unitary-solvent system, the key factor was the T_{bp} of the solvent(Fig. 4(a)), followed by γ and η in sequence, which was in good coordination with the experimental result. For the binary-solvent systems, it can be seen that ΔT_{bp} took the first place in the three systems in spite of different major solvents used (Fig. 4(b), (c), (d)), whereas the surface tension and viscosity played a less dominating role, indicating the great importance of ΔT_{bp}^*. However, the order of $\Delta\gamma$ and $\Delta\eta$ varied in

different systems, which may be attributed to the properties of different major solvents. These RF models accurately predicted A in the unitary-solvent system, the binary-DCL-based system and the binary-BCH-based system with R^2 values achieving 0.956 7, 0.983 9 and 0.944 2, respectively. For A in the binary-OCH-based system, an R^2 value of 0.798 0 was obtained, indicating a less precise prediction which might be attributed to the similar profiles and thus the similar A inputs in this system. In addition, the RMSEs were small in four systems, indicating the acceptable precision.

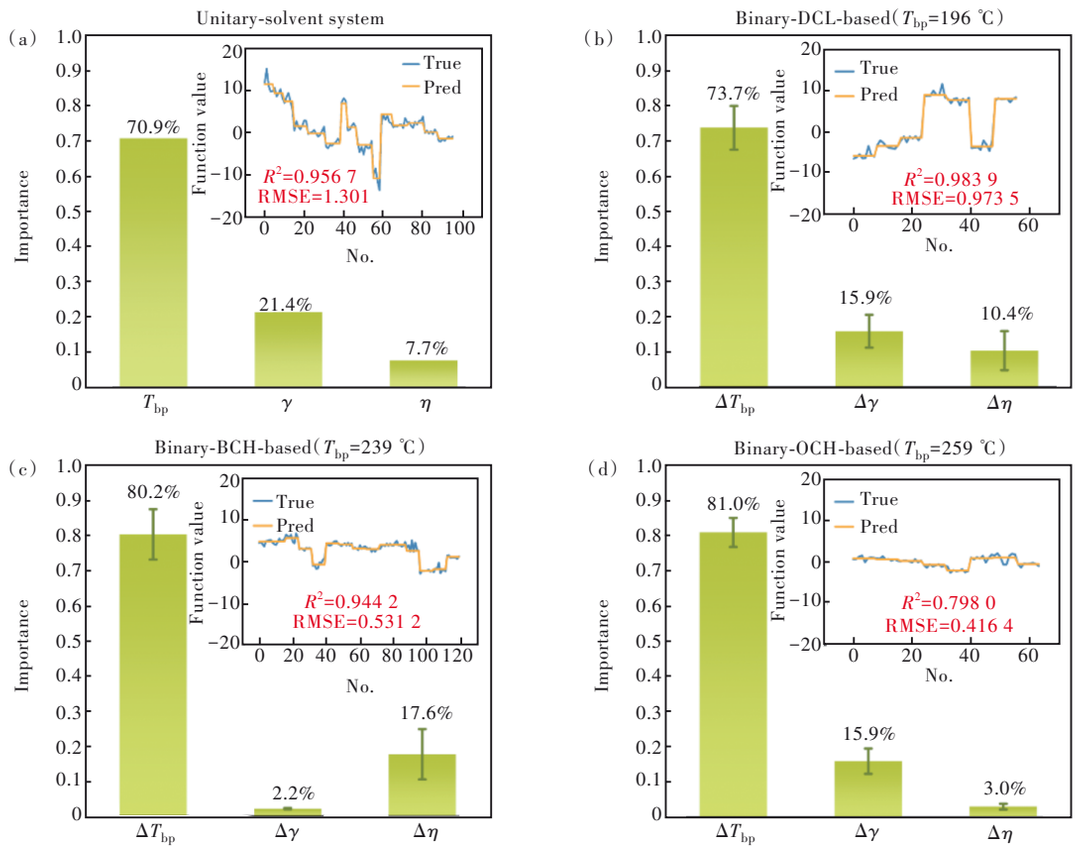

Fig.4　Importance of variables on surface curvature A. (a) Unitary-solvent system. (b) Binary-solvent system using decalin as the major solvent. (c) Binary-solvent system using bicyclohexane as the major solvent. (d) Binary-solvent using octylcyclohexane as the major solvent. Inserts: line plots for true values and predicted values of A for the corresponding group by RF models. R^2, coefficient of determination on test set data. RMSE, root mean square error on test set data.

Furthermore, Fig.5 shows the predictions of different input features on A in the unitary-solvent system (Fig. 5(a), (b), (c)) and the binary-solvent systems (Fig. 5(d), (e), (f)). In the unitary-solvent system, Fig. 5(a) firstly reveals that A was significantly affected by T_{bp}, which could be depicted by the significant differences in stratification at different T_{bp}. With T_{bp} rising, A gradually changed from positive to negative, implying that the film profile changed from concave to convex. Secondly, the effect of γ on A was related to T_{bp} (Fig. 5(b)). When T_{bp} was relatively low (190–260 ℃), high γ (> 29 mN/m) corresponded to high A, while low γ corresponded to low A; when T_{bp} was relatively high (> 260 ℃), the change of γ performed ignorable effect on A. Thirdly, the effect of η on A was related to T_{bp} and γ (Fig. 5(c)), where the change of η displayed almost no effect on A at any set of T_{bp} and γ. In binary-solvent systems, Fig. 5(d) reveals that a minor solvent with a higher boiling point promoted the formation of flat films because of the lower evaporation rate during the whole drying process. In addition, with a further increase of the major solvent's boiling point, the combinations that were applicable for a flat film formation increased, benefitting from the general slow evaporation, but this may lead to

lengthy drying during which other unideal situations, such as quenching and irregularities, may occur. Fig. 5(e) and Fig. 5(f) show the statistical influence of $\Delta\gamma$ and $\Delta\eta$ on A, from which we can see that there were no clear effects. These results can be corresponded to the RF importance analysis and were in full agreement with the experimental data and speculative conclusions.

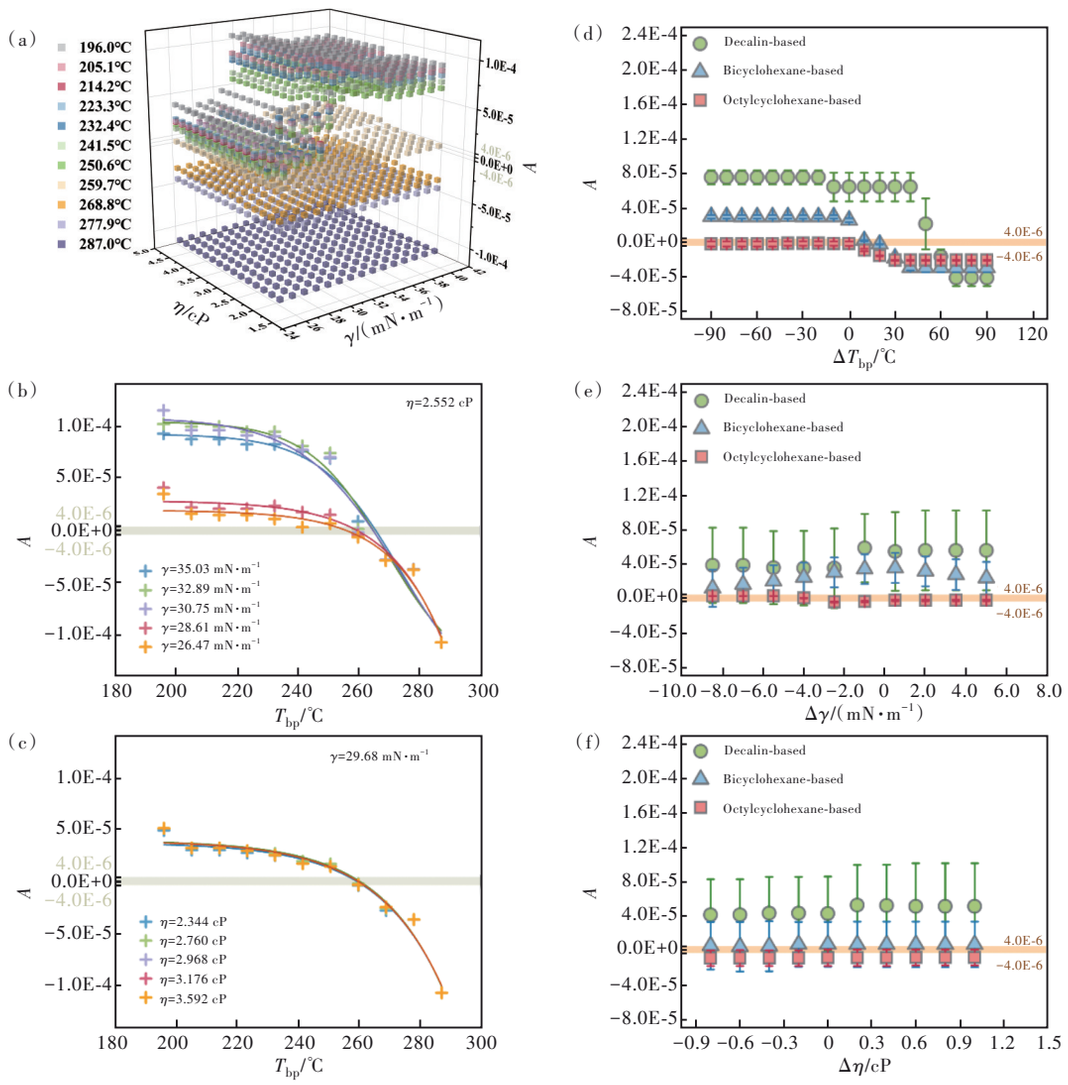

Fig.5 Prediction on surface curvature A by RF models. In the unitary-solvent system. (a)The trend of A with variable T_{bp}, γ and η of pure solvent. (b)The trend of A with variable T_{bp} under the same η and different γ. (c)The trend of A with variable T_{bp} under the same γ and different η. In the binary-solvent systems, the statistic trend of A with variable ΔT_{bp}(d), $\Delta\gamma$(e) and $\Delta\eta$(f).

As the result of a longer drying time, the surface irregularities were smoothened. For the unitary-solvent system, solvents with T_{bp} of 250–265 ℃ were preferred. For binary-solvent systems, minor solvents with T_{bp}^{*} of 250–260 ℃ were preferred, while a major solvent with a relatively lower boiling point would be better to offer high evaporation rate during the initial drying stage. In addition, machine learning unveiled the potential of big data analysis in ink engineering, especially considering the complexity and multiple affecting factors. Despite slight errors, such predictions enable effective tweaks of the properties free from labor-intensive trial and error.

4 Conclusion

We first identified the crucial parameter affecting the inkjet-printed QDs film profiles with experimental results as well as machine learning prediction

support. The results showed that the boiling point was more important compared with surface tension and viscosity. A boiling point range of 250-265 ℃ for the solvent in the unitary-solvent ink system or for the higher-boiling-point solvent in the binary-solvent ink systems can promisingly result in uniform films after drying.

In comparison with previous ink engineering methods, highlighting boiling point avoided complex calculations of the Marangoni number and viscous force, offering a simpler way to find a suitable solvent. In addition, machine learning developed models to conduct prediction and offer guidelines based on the great amount of data, enabling effective tweaks of the properties free from labor-intensive trial and error. Furthermore, it could help consider the multiple parameters related to film morphology including surface energy of substrate and concentration of QDs for finding out more internal clues, which performed as a promising potential trend in this field.

Consequently, this work demonstrated a simpler strategy for tailor-making inks to inkjet-print uniform QDs films and unveiled the potential of machine learning for simplifying ink engineering in the future. Furthermore, more precise fittings of the profiles and more diverse characterizations for the films are needed of further studies to construct more universal models.

Supplementary Information and Response Letter are available for this paper at: http://cjl.lightpublishing.cn/thesisDetails#10.37188/CJL.20230228.

References:

[1] LIU Z J, LIN C H, HYUN B R, *et al.* Micro-light-emitting diodes with quantum dots in display technology [J]. *Light: Sci. Appl.*, 2020, 9: 83.

[2] LEE E, WANG C M, YUREK J, *et al.* A new frontier for quantum dots in displays [J]. *Inf. Disp.*, 2018, 34(6): 10-31.

[3] KAÇAR R, SERIN R B, UÇAR E, *et al.* A review of high-end display technologies focusing on inkjet printed manufacturing [J]. *Mater. Today Commun.*, 2023, 35: 105534.

[4] SHU Y F, LIN X, QIN H Y, *et al.* Quantum dots for display applications [J]. *Angew. Chem. Int. Ed.*, 2020, 59(50): 22312-22323.

[5] MOON H, LEE C, LEE W, *et al.* Stability of quantum dots, quantum dot films, and quantum dot light-emitting diodes for display applications [J]. *Adv. Mater.*, 2019, 31(34): 1804294.

[6] SUN Y Z, JIANG Y B, SUN X W, *et al.* Beyond OLED: efficient quantum dot light-emitting diodes for display and lighting application [J]. *Chem. Rec.*, 2019, 19(8): 1729-1752.

[7] JANG H J, LEE J Y, BAEK G W, *et al.* Progress in the development of the display performance of AR, VR, QLED and OLED devices in recent years [J]. *J. Inf. Disp.*, 2022, 23(1): 1-17.

[8] LAN L H, ZOU J H, JIANG C B, *et al.* Inkjet printing for electroluminescent devices: emissive materials, film formation, and display prototypes [J]. *Front. Optoelectron.*, 2017, 10(4): 329-352.

[9] BAI J Y, HU H L, YU Y S, *et al.* Achieving high performance InP quantum dot light-emitting devices by using inkjet printing [J]. *Org. Electron.*, 2023, 113: 106705.

[10] BUKOWSKI T J, SIMMONS J H. Quantum dot research: current state and future prospects [J]. *Crit. Rev. Solid State Mater. Sci.*, 2002, 27(3-4): 119-142.

[11] JANG E, JANG H. Review: quantum dot light-emitting diodes [J]. *Chem. Rev.*, 2023, 123(8): 4663-4692.

[12] WEI C T, SU W M, LI J T, *et al.* A universal ternary-solvent-ink strategy toward efficient inkjet-printed perovskite quantum dot light-emitting diodes [J]. *Adv. Mater.*, 2022, 34(10): 2107798.

[13] WANG J H, DONG T, ZHONG Z M, *et al.* Uniform inkjet-printed films with single solvent [J]. *Thin Solid Films*, 2018, 667: 21-27.

[14] HAN J, KO D, PARK M, *et al.* Toward high-resolution, inkjet-printed, quantum dot light-emitting diodes for next-generation displays [J]. *J. Soc. Inf. Disp.*, 2016, 24(9): 545-551.

[15] DEEGAN R D, BAKAJIN O, DUPONT T F, *et al*. Capillary flow as the cause of ring stains from dried liquid drops [J]. *Nature*, 1997, 389(6653): 827-829.

[16] SEFIANE K. Patterns from drying drops [J]. *Adv. Colloid Interface Sci.*, 2014, 206: 372-381.

[17] KOVALCHUK N M, TRYBALA A, STAROV V M. Evaporation of sessile droplets [J]. *Curr. Opin. Colloid Interface Sci.*, 2014, 19(4): 336-342.

[18] WILSON S K, D'AMBROSIO H M. Evaporation of sessile droplets [J]. *Annu. Rev. Fluid Mech.*, 2023, 55: 481-509.

[19] EALES A D, ROUTH A F, DARTNELL N, *et al*. Evaporation of pinned droplets containing polymer: an examination of the important groups controlling final shape [J]. *AIChE J.*, 2015, 61(5): 1759-1767.

[20] WANG Z Y, OREJON D, TAKATA Y, *et al*. Wetting and evaporation of multicomponent droplets [J]. *Phys. Rep.*, 2022, 960: 1-37.

[21] MAN X K, DOI M. Vapor-induced motion of liquid droplets on an inert substrate [J]. *Phys. Rev. Lett.*, 2017, 119(4): 044502.

[22] MAMPALLIL D, ERAL H B. A review on suppression and utilization of the coffee-ring effect [J]. *Adv. Colloid Interface Sci.*, 2018, 252: 38-54.

[23] BRUTIN D. *Droplet Wetting and Evaporation: From Pure to Complex Fluids* [M]. London: Academic Press, 2015.

[24] WILLIAMS A G L, KARAPETSAS G, MAMALIS D, *et al*. Spreading and retraction dynamics of sessile evaporating droplets comprising volatile binary mixtures [J]. *J. Fluid Mech.*, 2021, 907: A22.

[25] KARPITSCHKA S, LIEBIG F, RIEGLER H. Marangoni contraction of evaporating sessile droplets of binary mixtures [J]. *Langmuir*, 2017, 33(19): 4682-4687.

[26] PAHLAVAN A A, YANG L S, BAIN C D, *et al*. Evaporation of binary-mixture liquid droplets: the formation of picoliter pancakelike shapes [J]. *Phys. Rev. Lett.*, 2021, 127(2): 024501.

[27] PARK J, MOON J. Control of colloidal particle deposit patterns within picoliter droplets ejected by ink-jet printing [J]. *Langmuir*, 2006, 22(8): 3506-3513.

[28] JIANG C B, ZHONG Z M, LIU B Q, *et al*. Coffee-ring-free quantum dot thin film using inkjet printing from a mixed-solvent system on modified ZnO transport layer for light-emitting devices [J]. *ACS Appl. Mater. Interfaces*, 2016, 8(39): 26162-26168.

[29] LIU Y, LI F S, XU Z W, *et al*. Efficient all-solution processed quantum dot light emitting diodes based on inkjet printing technique [J]. *ACS Appl. Mater. Interfaces*, 2017, 9(30): 25506-25512.

[30] XIONG X Y, WEI C T, XIE L M, *et al*. Realizing 17.0% external quantum efficiency in red quantum dot light-emitting diodes by pursuing the ideal inkjet-printed film and interface [J]. *Org. Electron.*, 2019, 73: 247-254.

[31] JIA S Q, TANG H D, MA J R, *et al*. High performance inkjet-printed quantum-dot light-emitting diodes with high operational stability [J]. *Adv. Opt. Mater.*, 2021, 9(22): 2101069.

[32] CHEN M, XIE L M, WEI C T, *et al*. High performance inkjet-printed QLEDs with 18.3% EQE: improving interfacial contact by novel halogen-free binary solvent system [J]. *Nano Res.*, 2021, 14(11): 4125-4131.

[33] 熊雪莹, 魏昌庭, 苏文明, 等. 喷墨打印镉基绿光量子点发光二极管及其界面 [J]. 发光学报, 2019, 40(10): 1274-1280.
XIONG X Y, WEI C T, SU W M, *et al*. Performance and interface of inkjet-printed cadmium (Cd)-based green quantum dot light-emitting diodes [J]. *Chin. J. Lumin.*, 2019, 40(10): 1274-1280. (in Chinese)

[34] 郭标, 穆兰, 罗宇, 等. 喷墨打印量子点墨水调控 [J]. 发光学报, 2021, 42(6): 880-888.
GUO B, MU L, LUO Y, *et al*. Ink formulation of quantum dots in ink jet printing [J]. *Chin. J. Lumin.*, 2021, 42(6): 880-888. (in Chinese)

[35] YANG X Y, JIANG Z C, LYU P H, *et al*. Deposition pattern of drying droplets [J]. *Commun. Theor. Phys.*, 2021, 73(4): 047601.

[36] BREIMAN L. Random forests [J]. *Mach. Learn.*, 2001, 45(1): 5-32.

[37] NICODEMUS K K. Letter to the editor: on the stability and ranking of predictors from random forest variable importance measures [J]. *Briefings Bioinf.*, 2011, 12(4): 369-373.

[38] BIAU G, SCORNET E. A random forest guided tour [J]. *Test*, 2016, 25(2): 197-227.

[39] SOLTMAN D, SMITH B, KANG H K, *et al*. Methodology for inkjet printing of partially wetting films [J]. *Langmuir*,

2010, 26(19): 15686-15693.

[40] XIE Q G, HARTING J. From dot to ring: the role of friction in the deposition pattern of a drying colloidal suspension droplet [J]. *Langmuir*, 2018, 34(18): 5303-5311.

[41] LARSON R G. Twenty years of drying droplets [J]. *Nature*, 2017, 550(7677): 466-467.

[42] ZHONG X, CRIVOI A, DUAN F. Sessile nanofluid droplet drying [J]. *Adv. Colloid Interface Sci.*, 2015, 217: 13-30.

[43] LARSON R G. Transport and deposition patterns in drying sessile droplets [J]. *AIChE J.*, 2014, 60(5): 1538-1571.

[44] TESHIGAWARA R, ONUKI A. Spreading with evaporation and condensation in one-component fluids [J]. *Phys. Rev. E*, 2010, 82(2): 021603.

[45] KRAINER S, SMIT C, HIRN U. The effect of viscosity and surface tension on inkjet printed picoliter dots [J]. *RSC Adv.*, 2019, 9(54): 31708-31719.

[46] 雷霄霄, 叶芸, 林楠, 等. 喷墨打印量子点薄膜的形貌控制 [J]. 光子学报, 2019, 48(6): 0616001.
LEI X X, YE Y, LIN N, *et al.* Morphology controlling of quantum dots thin films prepared by inkjet printing [J]. *Acta Photon. Sinica*, 2019, 48(6): 0616001. (in Chinese)

欧家琦(1999-),女,广东东莞人,硕士研究生,2021年于华南理工大学获得学士学位,主要从事喷墨打印量子点薄膜与器件的研究。
E-mail: 527381016@qq.com

彭俊彪(1962-),男,山东宁津人,博士,教授,1993年于中国科学院长春物理研究所获得博士学位,主要从事发光显示器件与物理的研究。
E-mail: psjbpeng@scut.edu.cn